Supplementary Information (SI) for Energy & Environmental Science.

Supplementary Information

Dynamic Cathode Interlayer for Ultralow Self-Discharge and High Iodide Utilization in Zinc-Iodine Batteries

Junming Kang#[a], Jiajia Zhang#[a], Wang Wan[b], Zhimin Zhai[a], Ganxiong Liu[b], Ying Ge[a], Lequan Wang[a], Chao Wang*[b], and Hongbin Lu*[ac]

[a] State Key Laboratory of Molecular Engineering of Polymers, Department of Macromolecular Science, Fudan University, Shanghai 200438, China.

E-mail: hongbinlu@fudan.edu.cn

[b] School of Materials Science and Engineering, Tongji University, Shanghai 201804, China.

E-mail: chaow@tongji.edu.cn

[c] Yiwu Research Institute of Fudan University, Yiwu 322000, Zhejiang, China.

# These authors contributed equally to this work.

Experimental Section

Preparation of the cathode and electrolyte

All chemicals were used directly without any post-treatments. Iodine (I_2, AR, 99.8%), Potassium iodide (KI, AR, >99.0%), Tetramethylammonium iodide, (TMAI, 98%), Zinc sulfate heptahydrate ($ZnSO_4 \cdot 7H_2O$, AR), and Sodium sulfate ($NaSO_4$, AR, 99%) were purchased from Aladdin (Shanghai, China). Porous carbon (PC, YP-50F) was obtained from Saibo electrochemical materials store. The cathode composite was prepared by mixing and heating PC and I_2 at 120 °C for 120 minutes in a Pyrex tube. The mass ratio of I_2 in the composite is approximately 50%. The electrodes were prepared by blending the cathode composite with 10% wt. PTFE and a small amount of ethanol, then rolling the mixture into membranes. Subsequently, the membranes were subjected to heating at 60 °C for 3 hours. Afterward, the membranes were punched into 10 mm × 10 mm squares and compressed onto Ti grid collectors. The precipitate cathode was obtained by grinding the precipitates and PC in a 1: 1 mass ratio, followed by the same manufacturing process. For the TMAI electrolyte, $ZnSO_4 \cdot 7H_2O$ and TMAI were directly dissolved in the deionized water to obtain a 2 M $ZnSO_4$ + 0.1 (0.01, 0.05, 0.2) M TMAI aqueous electrolyte. The KI and BE electrolytes were obtained by dissolving 2 M $ZnSO_4$ + 0.1 M KI and 2 M $ZnSO_4$ in deionized water, respectively.

Characterization

Scanning electron microscopy (SEM) was conducted on Zeiss Gemini SEM500 equipped with an Aztec X-Max Extreme energy dispersive spectrometer to characterize the morphology and element distribution. Ultraviolet-visible spectra (UV-vis) were acquired on Perkin-Elmer Lambda750. Raman spectra were recorded on Renishaw In Via Qontor with a laser of 532 nm. Fourier transform infrared (FTIR) spectra were obtained by Thermofisher Nicolet 6700. X-ray photoelectron spectroscopy (XPS) spectra were collected on PHI Genesis 500. X-ray diffraction (XRD) measurements were performed on Rigaku Smatlab 9KW with Cu-Kα radiation. Thermogravimetry (TG) tests were carried out on Mettler Toledo TGA 1. The zeta potentials were measured using Malvern Instruments ZS90.

Electrochemical measurement

The electrochemical properties were measured at room temperature by using CR2016 coin-type cells, assembled in an air atmosphere. The batteries were assembled with a composite iodine cathode, a 100 μm zinc anode, 100 μL electrolyte, and a glass fiber separator. For the low N/P ratio cells, the zinc anode was 10μm. For the pouch-type cells, the zinc anode was 20 μm, and the electrolyte was 45 μL cm^{-2}. The average mass loadings of iodine were about 6-8 mg cm^{-2} for coin-type cells and 15 mg cm^{-2} for low N/P ratio and pouch-type cells. The galvanostatic charge-discharge (GCD) tests were performed on a Neware battery testing system at different current densities with a voltage window of 0.6 to 1.6 V. The cyclic voltammetry (CV), chronoamperometry (CA), linear sweep voltammetry (LSV), alternating current voltammetry (ACV), and electrochemical impedance spectra (EIS) tests were conducted on CHI660E electrochemical station. In the tests for hydrogen evolution overpotentials, electric double layer (EDL) capacitances and differential capacitances (C_s), we replaced $ZnSO_4$ with Na_2SO_4 in the electrolytes to prevent interference from the Faradic current of Zn^{2+}. The calculation of specific capacities was based on the mass loading of iodine in cathodes. The electrochemical performance of precipitates was characterized by employing the precipitate cathode and the 2 M $ZnSO_4$ electrolyte. The specific capacity was calculated based on the mass loading of the precipitates, which is around 5 mg cm^{-2}.

Quantum chemical calculation

All the quantum chemical calculations were performed using the Gaussian 09 software package.[1] Structural optimization and electronic properties were determined using the b3lyp functional with the def2-TZVP basis set (empirical dispersion correction GD3(BJ)).[2–5] The binding energy (E_b) was calculated by equation (1):

$$E_b = E_S - E_{TMA} - E_I \tag{1}$$

where the E_S is the energy of the optimized system; E_{TMA} is the energy of $TMAI^+$ cation; E_I is the energy of iodine species.

Density functional theory (DFT) calculation

In this study, all density functional theory (DFT) calculations were conducted using the Vienna Ab initio Simulation Package (VASP)[6,7]. The Perdew−Burke−Ernzerhof (PBE) generalized gradient approach (GGA)[8] was employed to describe the exchange-correlation potential. The electron-ion interactions were modeled using the projector augmented wave (PAW) method[9]. A cut-off energy of 400 eV was used for all DFT calculations, and the 2×2×1 Gamma-centered Monkhorst-Pack grids k-points were selected to sample the Brillouin zone integration. The convergence criteria for the self-consistent iteration were set to 10^{-4} eV for energy and 0.05 eV $Å^{-1}$ for force. The DFT-D3 method was applied to account for van der Waals (vdW) interactions[10].

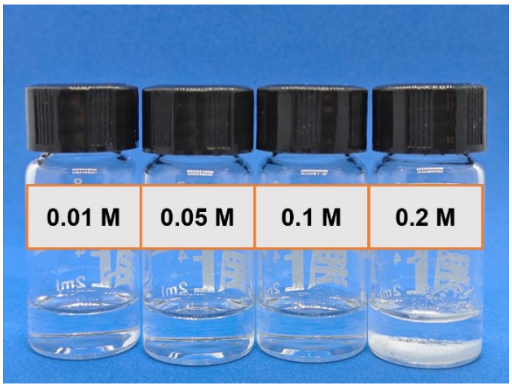

Fig. S1 Optical photograph of electrolytes containing different amounts of TMAI. Notably, It is beyond the solubility limit at 0.2 M TMAI.

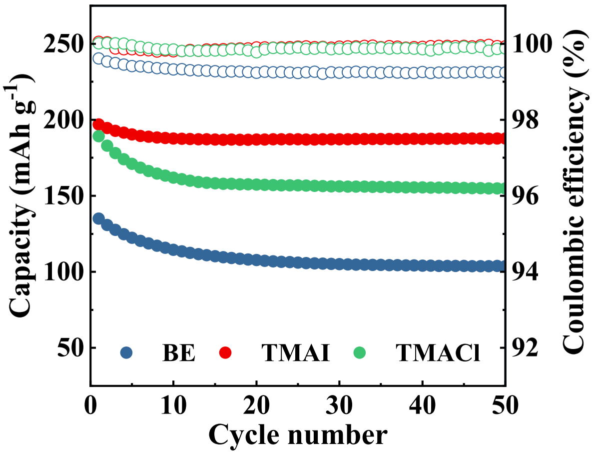

Fig. S2 Discharge capacity and Coulombic efficiency of batteries with different additives.

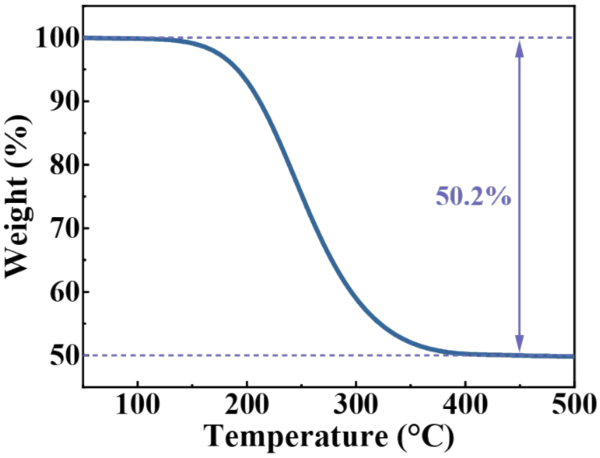

Fig. S3 TG curve of the cathode composite.

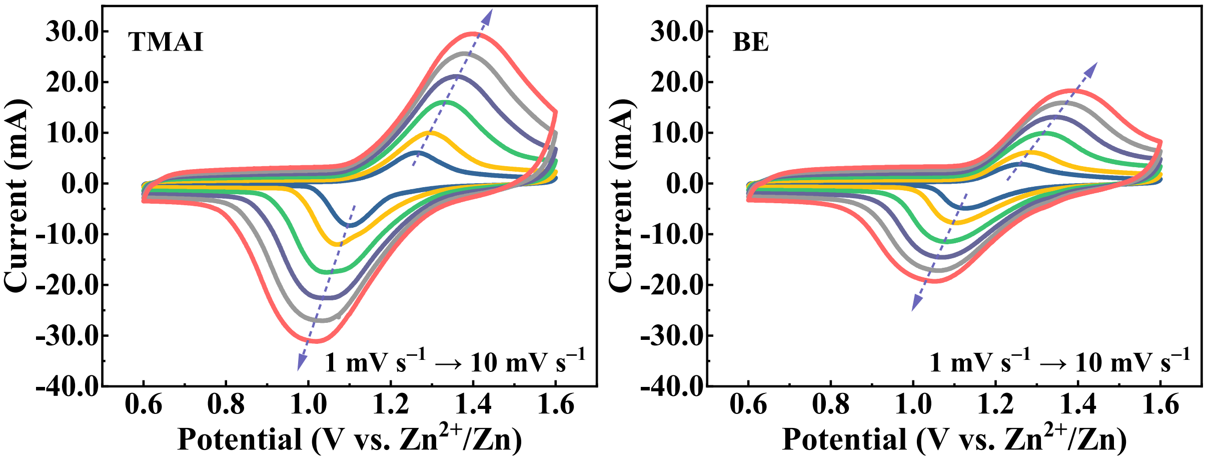

Fig. S4 CV curves of cells with different electrolytes.

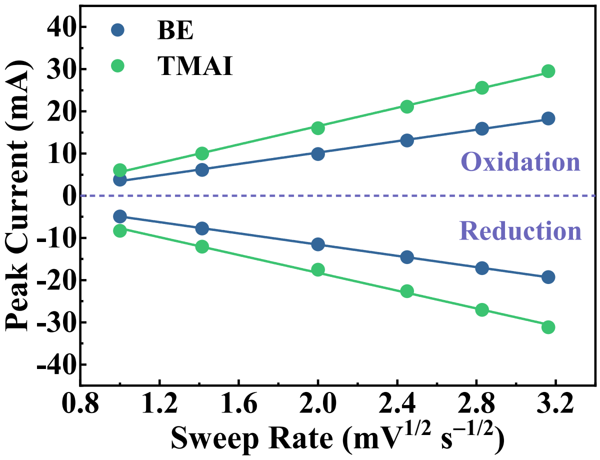

Fig. S5 Relationship between peak currents and sweep rates.

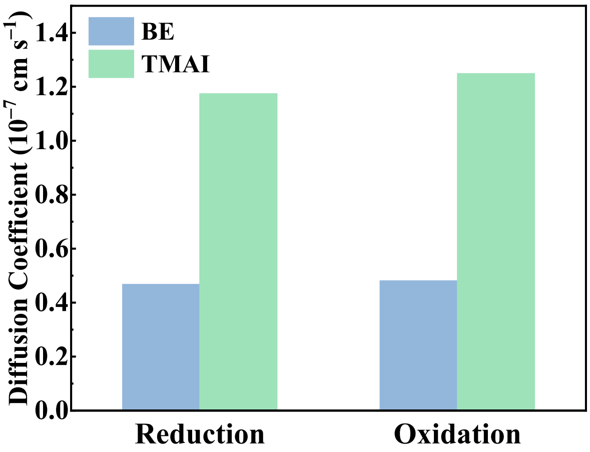

Fig. S6 Diffusion coefficients of the cells with different electrolytes.

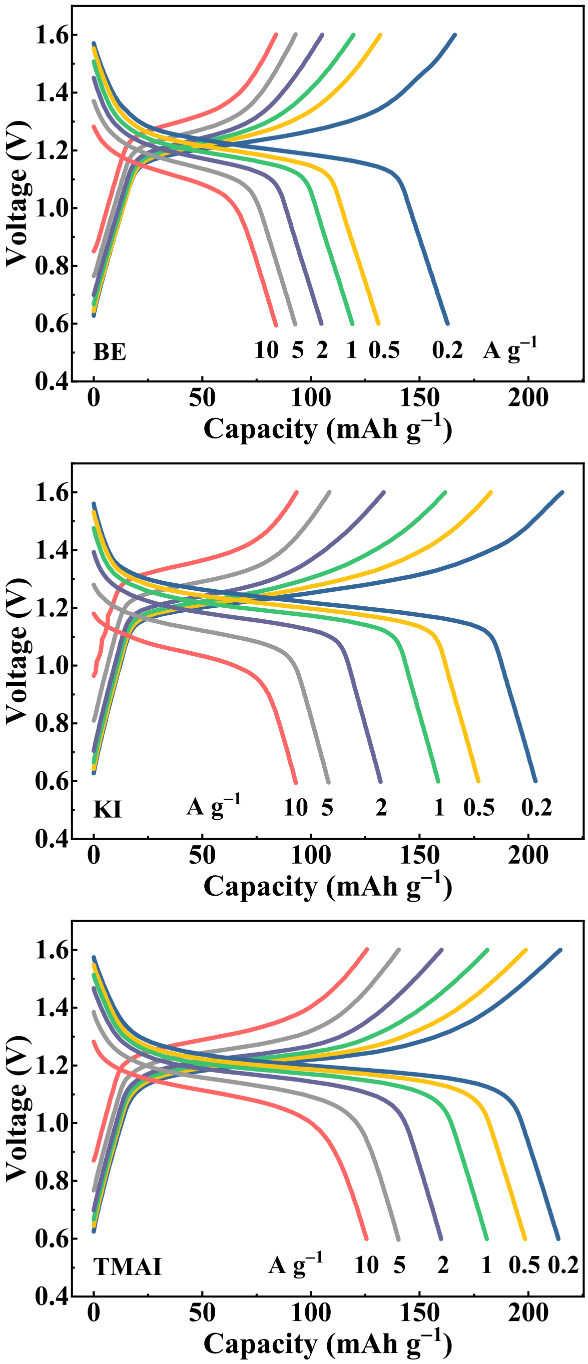

Fig. S7 GCD curves of cells with different electrolytes.

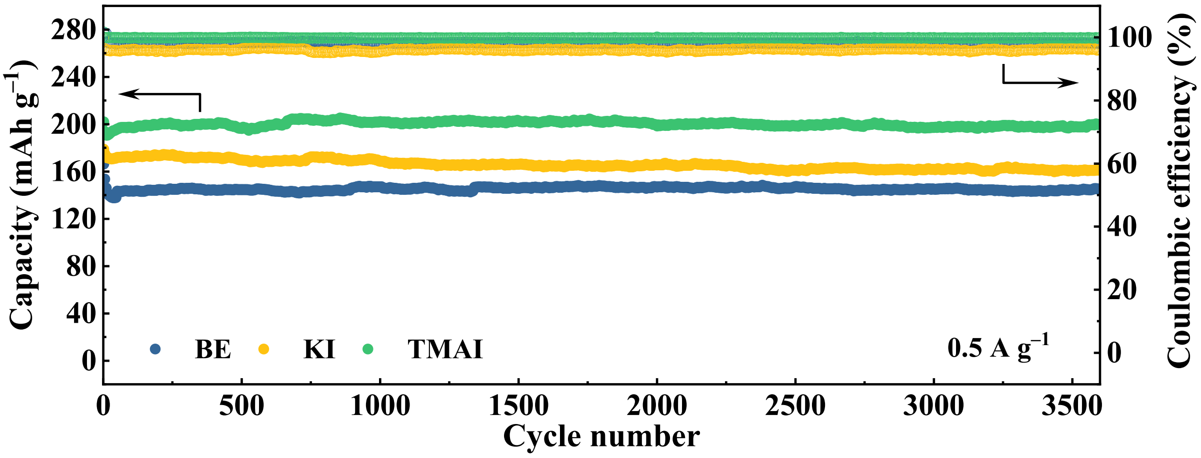

Fig. S8 Cycle stability of the cells with different electrolytes at 0.5 A g^{-1}.

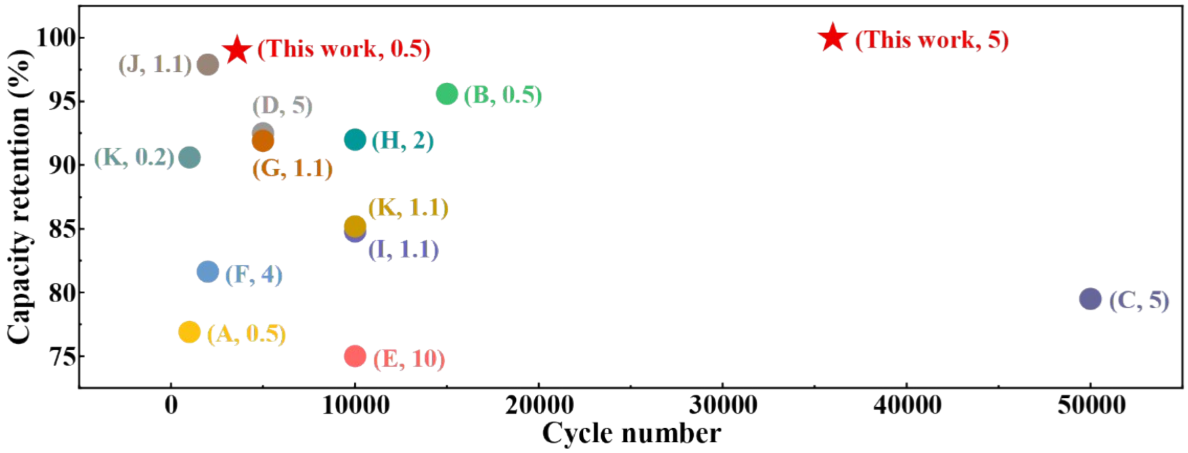

Fig. S9 Comparison of cycle stability of this work to other reports. The references in manuscript and current densities (mA g^{-1}) are given in brackets. A: Ref.28; B: Ref.29; C: Ref.30; D: Ref.31; E: Ref.32; F: Ref.38; G: Ref.39; H: Ref.40; I: Ref.41; J: Ref.42; K: Ref.43.

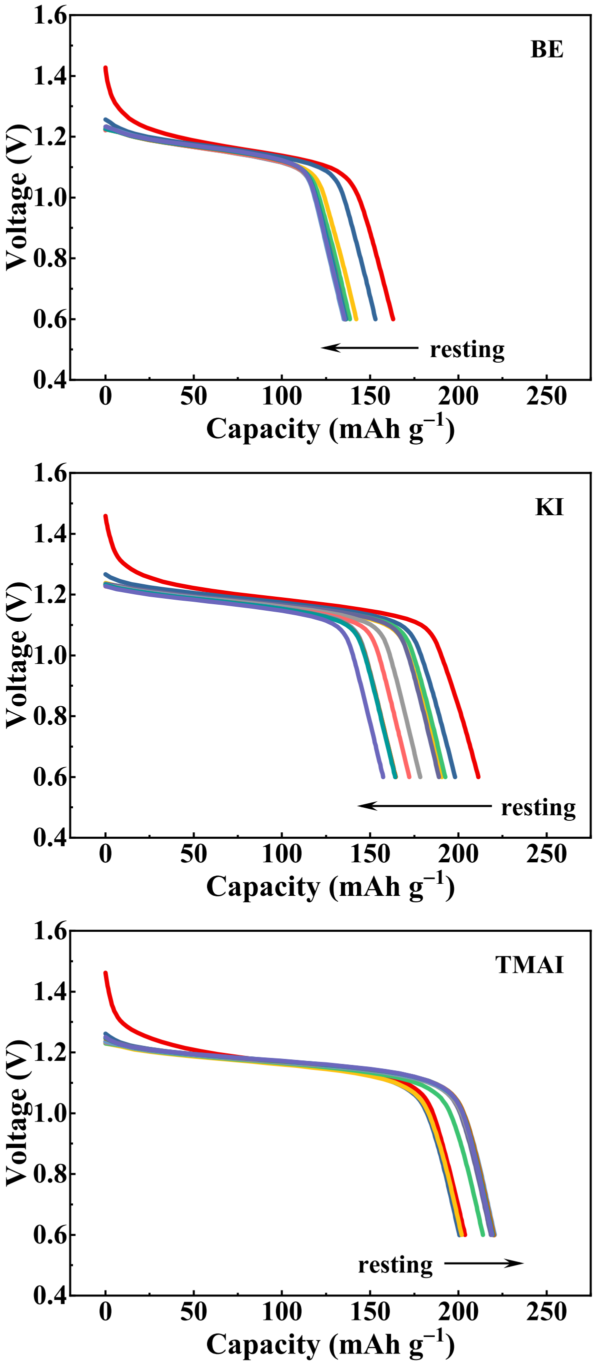

Fig. S10 Discharge curves of the cells with different electrolytes after resting different time.

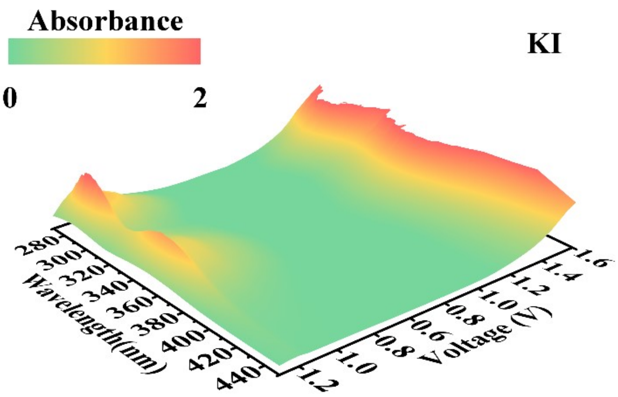

Fig. S11 In-situ UV-vis spectra of the KI electrolyte.

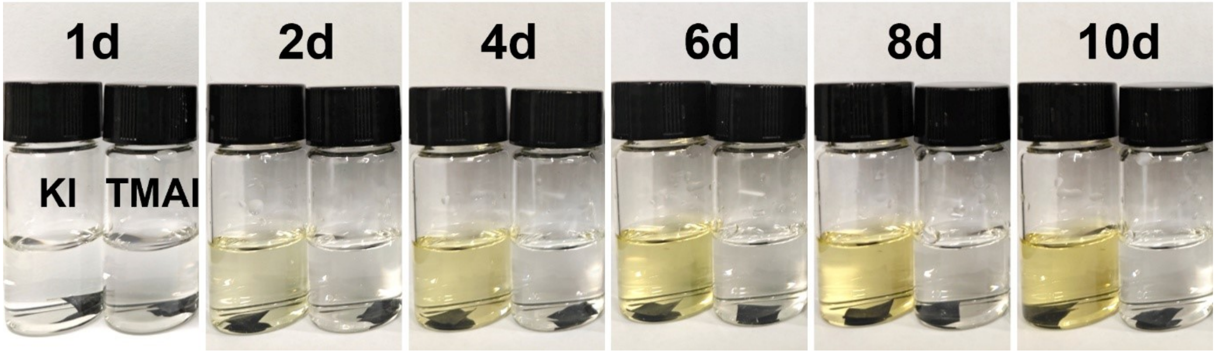

Fig. S12 Optical photographs of KI and TMAI electrolytes after immersing iodine cathode for different days.

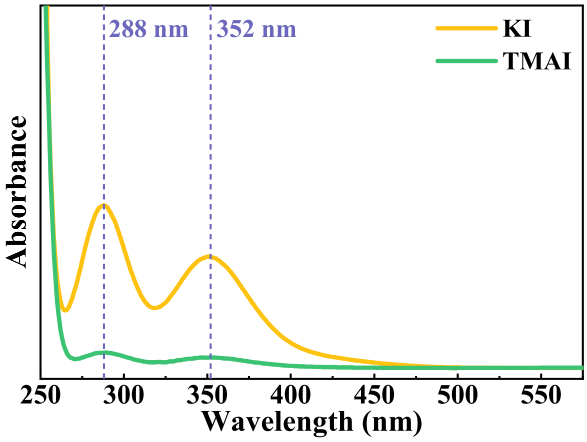

Fig. S13 UV-vis spectra of KI and TMAI electrolytes after immersing iodine cathode for 10 days.

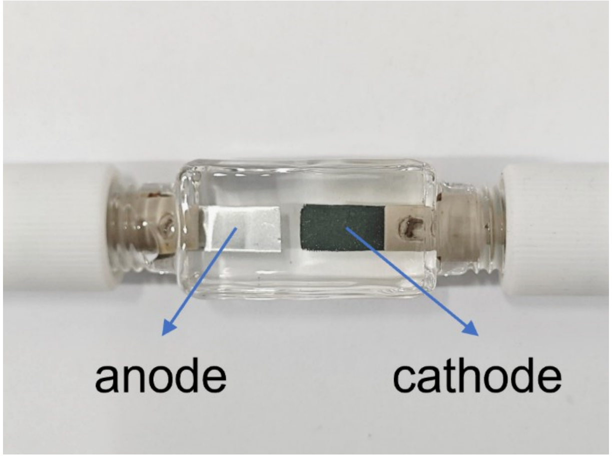

Fig. S14 In-situ optical device for monitoring evolution of the cathode interlayer.

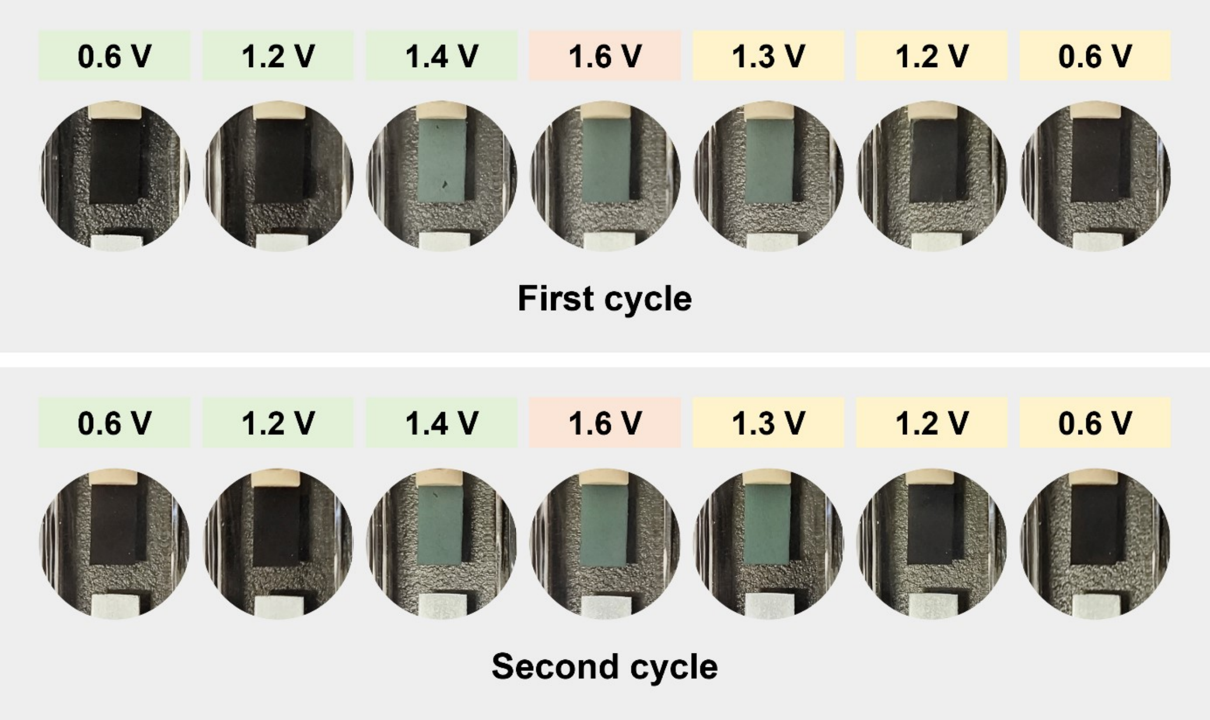

Fig. S15 In-situ optical photographs of the cathode interlayer during cycling.

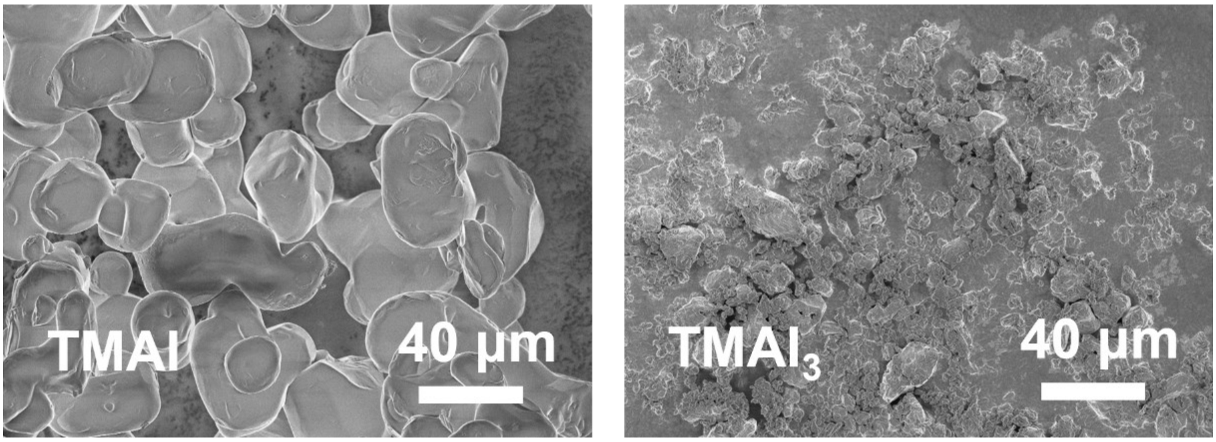

Fig. S16 SEM images of TMAI and precipitates.

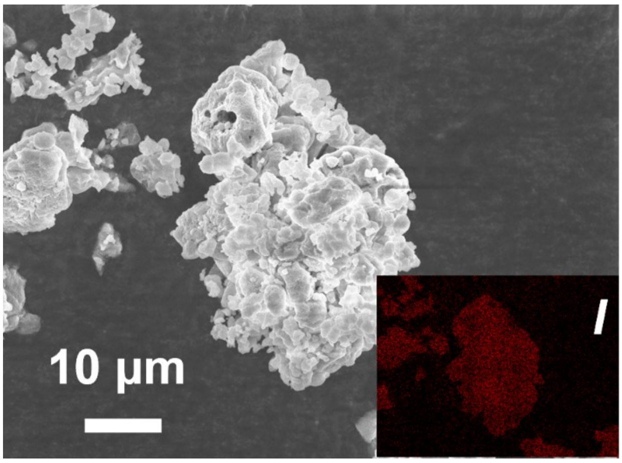

Fig. S17 EDS image of precipitates.

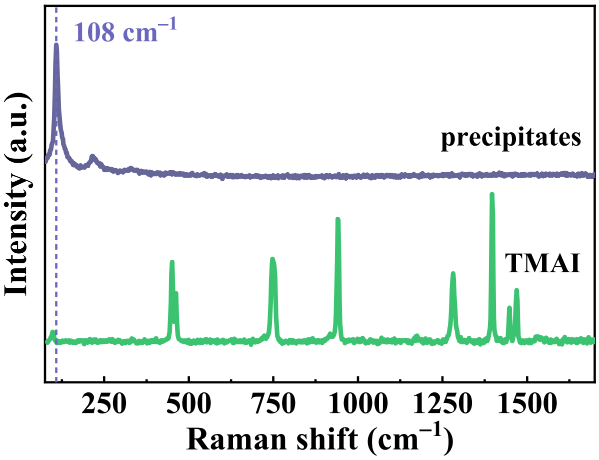

Fig. S18 Raman spectra of TMAI and precipitates.

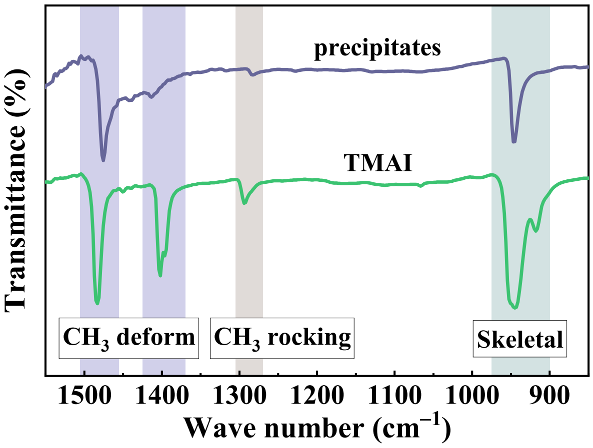

Fig. S19 FTIR spectra of TMAI and precipitates.

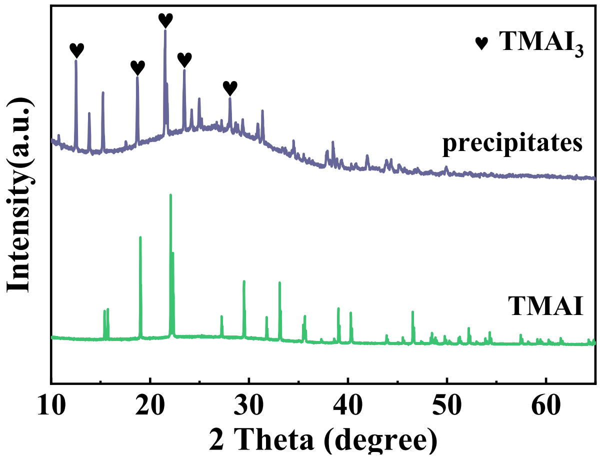

Fig. S20 XRD patterns of TMAI and precipitates.

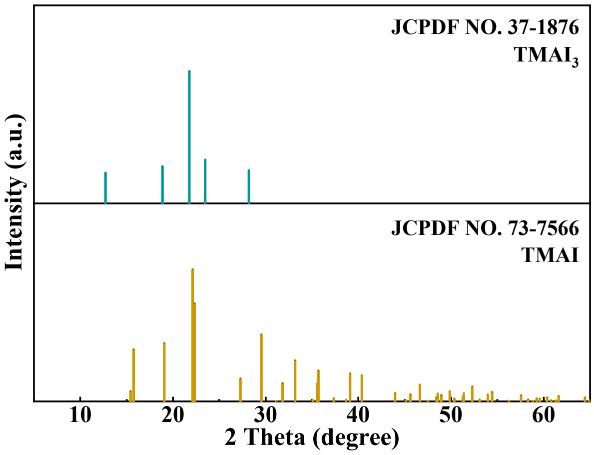

Fig. S21 JCPDF cards of TMAI and $TMAI_3$.

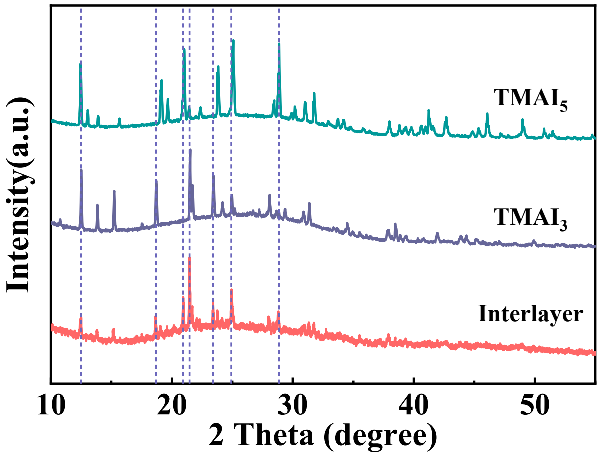

Fig. S22 XRD patterns of the interlayer, TMAI$_3$ and TMAI$_5$.

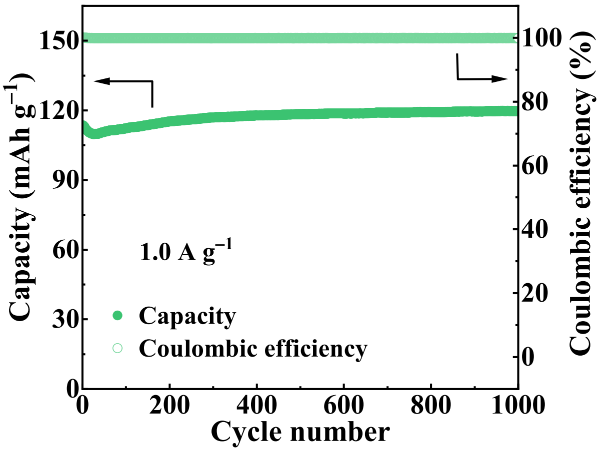

Fig. S23 Cycling performance of the precipitates.

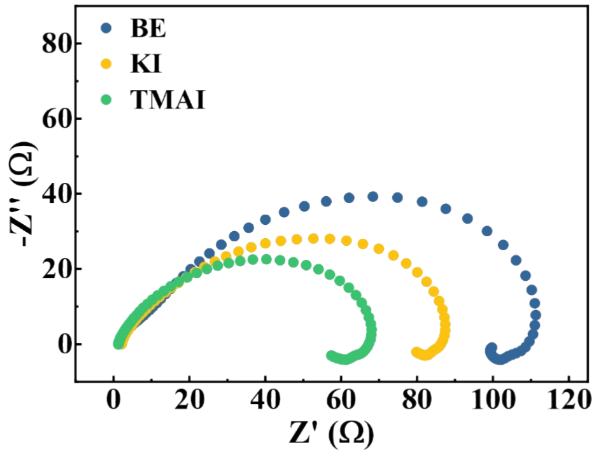

Fig. S24 EIS of zinc electrodes in different electrolytes.

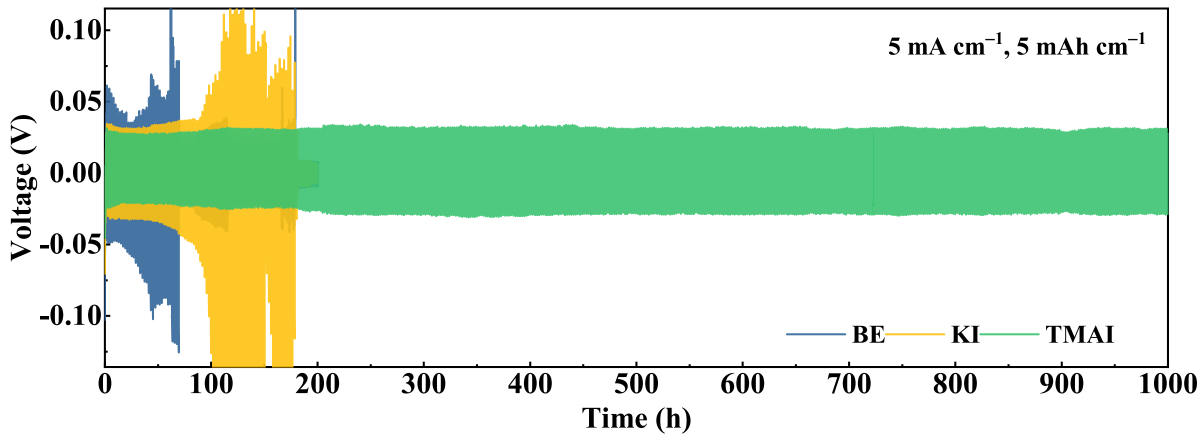

Fig. S25 Cycle stability of Zn||Zn symmetric cells.

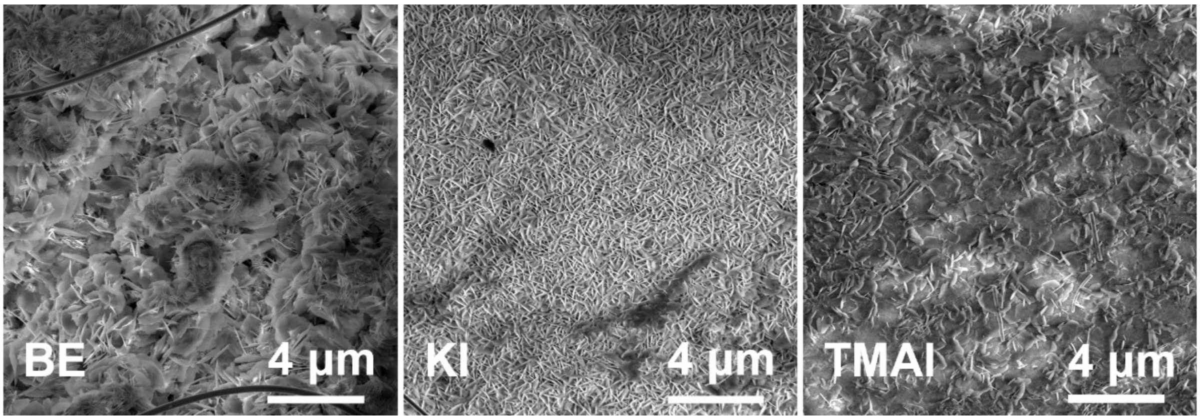

Fig. S26 SEM images of zinc anodes after deposition at 5 mA cm^{-2} and 5 mAh cm^{-2}.

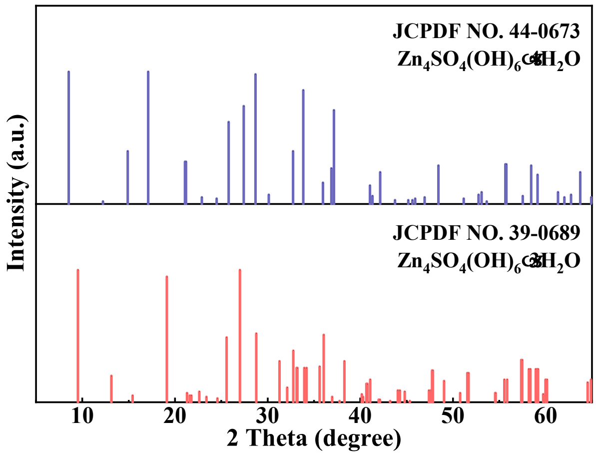

Fig. S27 JCPDF cards of basic zinc sulfate by-products.

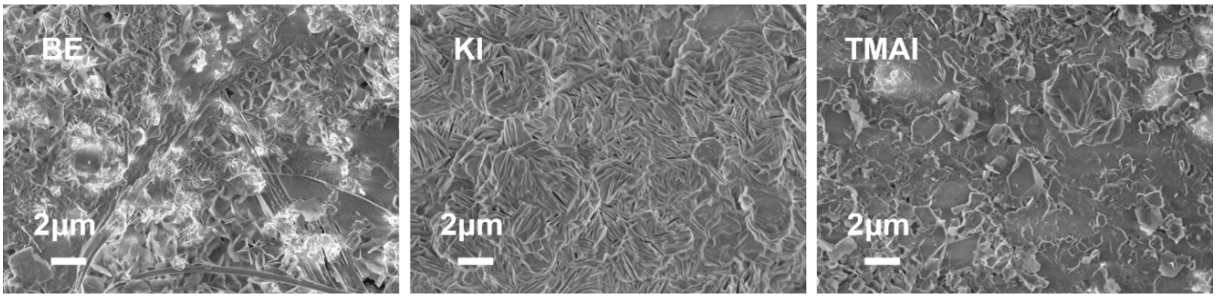

Fig. S28 SEM images of zinc anodes in full cells after 50 cycles at 5 A g^{-1}.

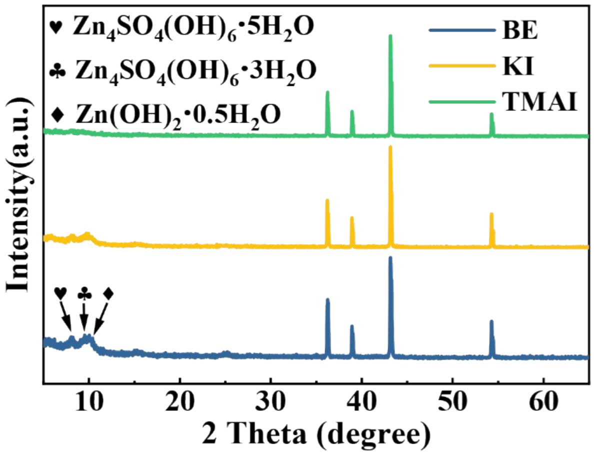

Fig. S29 XRD patterns of zinc anodes in full cells after 50 cycles at 5 A g^{-1}.

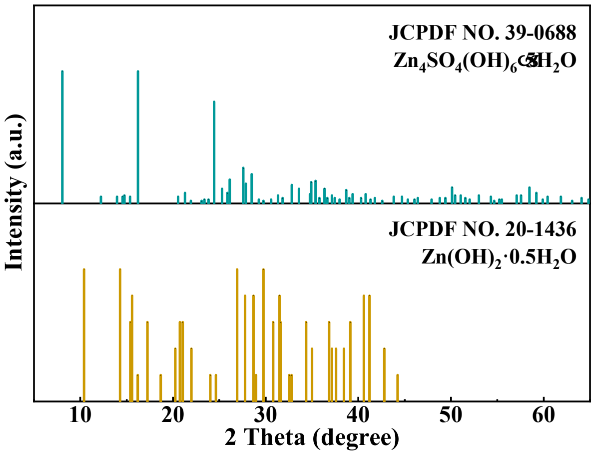

Fig. S30 JCPDF cards of basic zinc sulfate and zinc hydroxide by-products.

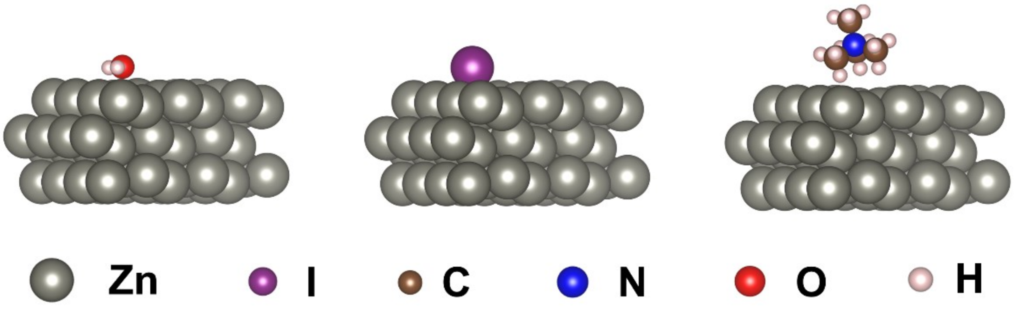

Fig. S31 Adsorption models of H_2O, I^- and TMA^+ on Zn (001) crystal planes.

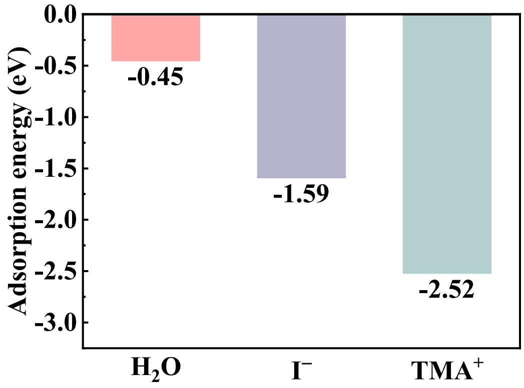

Fig. S32 Adsorption energies of H_2O, I^- and TMA^+ on Zn (001) crystal planes.

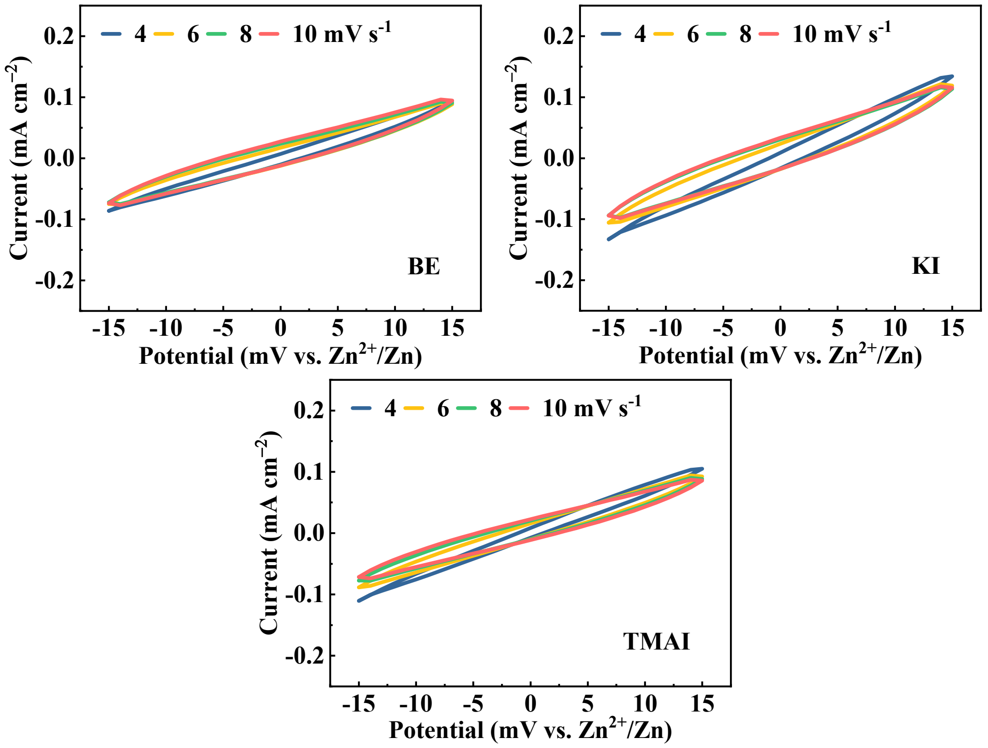

Fig. S33 CV curve of Zn||Zn symmetric cells with different Na_2SO_4 electrolytes.

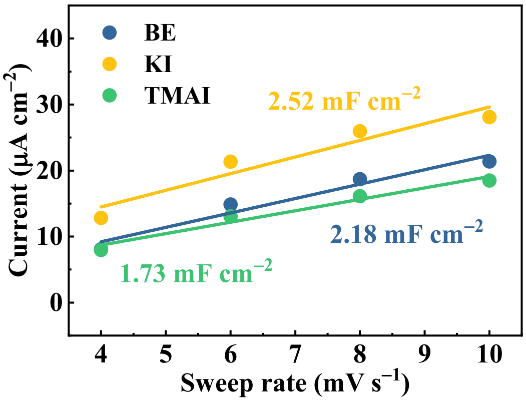

Fig. S34 Calculated EDL capacitances in different electrolytes containing Na_2SO_4.

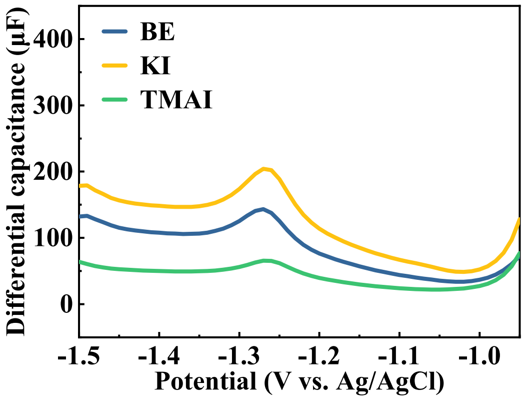

Fig. S35 Differential capacitance curves in different Na_2SO_4 electrolytes.

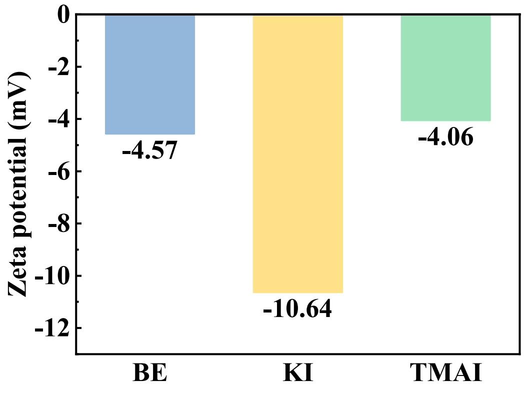

Fig. S36 Zeta potentials of zinc metal in different $ZnSO_4$ electrolytes.

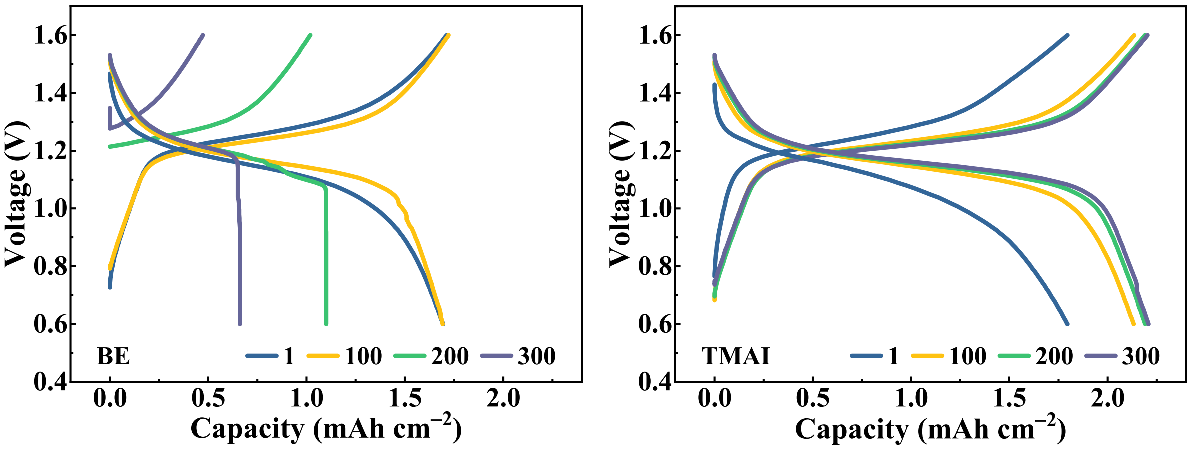

Fig. S37 GCD curves of the low N/P ratio full cells with different electrolytes.

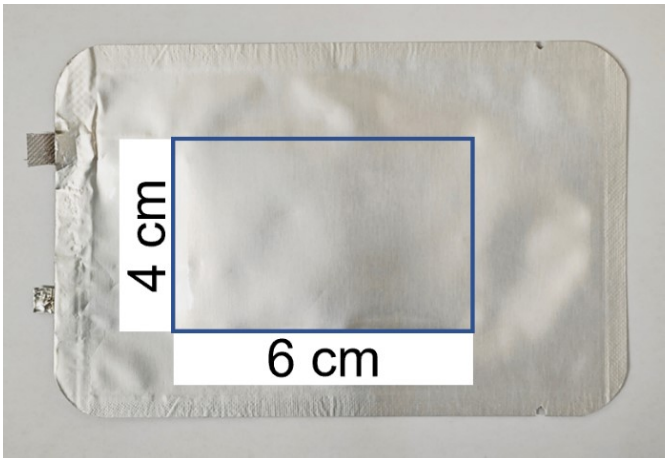

Fig. S38 Optical photograph of the 4 × 6 cm^2 pouch cell.

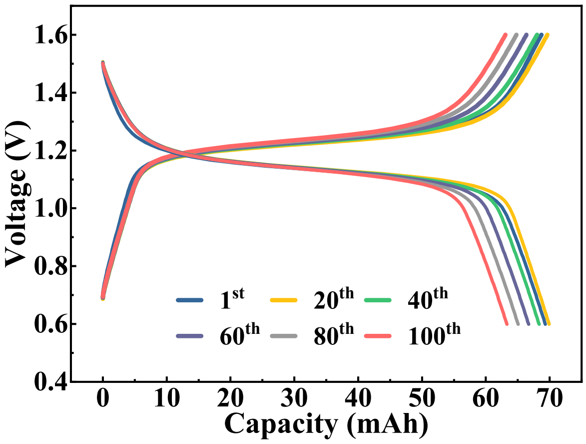

Fig. S39 GCD curves of the 4 × 6 cm^2 pouch-type cell.

References

1 G. Kresse and J. Furthmüller, *Comput. Mater. Sci.*, 1996, **6**, 15–50.

2 Y. Zhao and D. G. Truhlar, *Acc. Chem. Res.*, 2008, **41**, 157–167.

3 F. Weigend and R. Ahlrichs, *Phys. Chem. Chem. Phys.*, 2005, **7**, 3297–3305.

4 P. E. Blöchl, *Phys. Rev. B*, 1994, **50**, 17953–17979.

5 J. P. Perdew and W. Yue, *Phys. Rev. B*, 1986, **33**, 8800–8802.

6 G. Kresse and J. Hafner, *Phys. Rev. B*, 1993, **47**, 558–561.

7 G. Kresse and J. Hafner, *Phys. Rev. B*, 1994, **49**, 14251–14269.

8 J. P. Perdew, K. Burke and M. Ernzerhof, *Phys. Rev. Lett.*, 1996, **77**, 3865–3868.

9 G. Kresse and D. Joubert, *Phys. Rev. B*, 1999, **59**, 1758–1775.

10 S. Grimme, J. Antony, S. Ehrlich and H. Krieg, *J. Chem. Phys.*, 2010, **132**, 154104.